Frontal Interaction with Isolated Orography

BRIAN D. GROSS*

Atmospheric and Oceanic Sciences Program, Princeton University, Princeton, New Jersey

(Manuscript received 16 August 1993, in final form 19 October 1993)

ABSTRACT

The interaction of a three-dimensional cold front and an isolated orographic ridge is examined by means of primitive equation model simulations. The front evolves as part of a developing nonlinear baroclinic wave and propagates southward toward the ridge. Many of the features in this interaction, such as the anticyclonic distortion of the front, divergence and frontolysis on the windward slope, convergence and frontogenesis in the lee, and the frontogenetical forcing associated with tilting, have previously been captured by simulations of a passive scalar traversing a ridge.

It is shown that the ridge decelerates the cold postfrontal air and creates a high pressure anomaly on the windward slope. If this anomaly is strong enough, it accelerates air over the ridge peak in a shallow ageostrophic flow that possesses many features found in a gravity current. This current provides relatively strong surface frontogenesis through the convergence term, but cannot transport enough mass across the peak to weaken the anomalous high pressure. The cold air and pressure anomaly propagate eastward in a manner similar to a topographic Rossby wave. When the east ridge end is reached, the anomalous pressure gradient accelerates the flow into the lee, where frontogenesis occurs from shearing. The motion behind the front as it propagates over and around the ridge is distinctly unbalanced.

Blocking, as measured by the ratio of the mass flux around the ridge end to that over the peak, is determined by a Froude number that depends on the propagation speed of the front (i.e., the strength of the baroclinic wave) and the mountain height. Higher mountains or weaker waves tend to produce total blocking of the front, resulting in flow only around the east ridge end. Lower mountains and stronger waves produce frontogenesis patterns and frontal distortions that more closely resemble the passive scalar simulations.

1. Introduction

The interaction of fronts with orographic features has recently received a great deal of attention, in part because this interaction has been implicated in the generation of several important atmospheric circulation systems. These include lee cyclones (Tafferner 1990; Orlanski and Gross 1994); squall lines (Koch and Kocin 1991); and cold surges east of the Tibetan Plateau (Chang et al. 1983), the Rocky Mountains (Hartjenstein and Bleck 1991), Australia (Baines 1980), and the Pyrenees (Hoinka and Heimann 1988). Moreover, several experimental studies, including the Alpine Experiment (ALPEX) and the German Fronts Experiment (Hoinka and Volkert 1987), provide relatively detailed observations of this interaction. Indeed, an entire issue of *Meteorology and Atmospheric Physics* (Vol. 48, Nos. 1–4, 1992) has been devoted to the topic of fronts and orography.

An example of the retardation and distortion of a front approaching the Alps is shown in Fig. 1 (after Radinovic 1986). The surface pressure pattern shows strong high and rising pressures to the north of the Alpine massif at 0000 UTC (Fig. 1a). Six hours later (Fig. 1b), this high pressure has nosed southward around the east end of the Alps, with continuing pressure rises at the eastern extremity of this feature. This dipolar surface pressure distribution is rather common near the Alps (Chen and Smith 1988).

Both observational (e.g., Hoinka et al. 1990) and modeling (e.g., Williams et al. 1992) approaches have been employed to examine the interaction of fronts and orography, and reviews of these approaches and results are provided by Blumen (1992) and Egger and Hoinka (1992). However, with few exceptions (e.g., Schumann 1987), efforts to understand the basic physical mechanisms associated with the interaction of fronts and orography have focused on relatively simple two-fluid models of flow over orography (Davies 1984; Blumen 1992) or two-dimensional analyses of stratified flow over semi-infinite mountain ridges (Blumen and Gross 1987; Zehnder and Bannon 1988; Williams et al. 1992). The dynamics in these models are essentially governed by mass continuity constraints. For example in the Davies (1984) two-dimensional model,

* Current affiliation: Geophysical Fluid Dynamics Laboratory/ NOAA, Princeton University, Princeton, New Jersey.

Corresponding author address: Dr. Brian D. Gross, NOAA/ GFDL, Princeton University, P.O. Box 308, Princeton, NJ 08542.
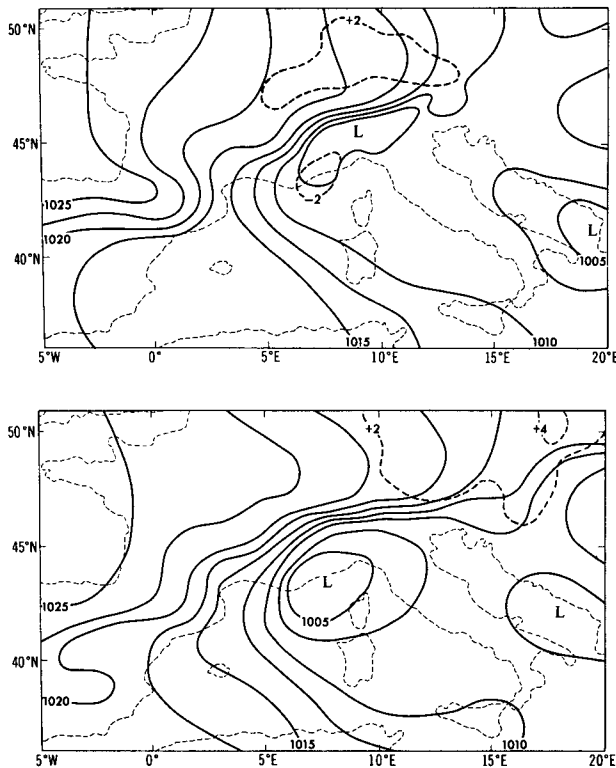
FIG. 1. Surface pressure (solid contours every 2.5 hPa), surface pressure tendency (dashed lines, R indicates a pressure rise and F a pressure fall, in units of hPa/3 h), and the analyzed front over the Alpine region on 30 April 1982 at (top) 0000 UTC and (bottom) 0600 UTC (Radinovic 1986).

frontal propagation speeds increase as the angle between the front and the ground decreases (Blumen 1992), and infinite propagation speeds occur when the slopes of the front and topography are equal. An extension of this model to three dimensions (Blumen 1992) produces an anticyclonic distortion of the front similar to that found in a passive scalar field that propagates over an isolated orographic feature (Blumen and Gross 1987).

Two-dimensional stratified models of frontal interaction with orography have shown that the interaction between the ageostrophic cross-frontal circulation and the circulation produced by flow over the ridge can weaken frontogenesis on the windward slope, where mass continuity requires flow divergence, and strengthen it on the lee slope, where mass continuity requires convergence. Williams et al. (1992) have shown that many of the properties of this interaction are quite similar to those revealed in relatively simple studies of passive scalars traversing orography. An extension to three dimensions (Schumann 1987) shows that an initially two-dimensional front can also undergo anticyclonic distortion as it is advected by the mountain anticyclone, as in Blumen's (1992) two-fluid

model. Schär (1990) has further shown that disturbances with the scale of a baroclinic lee wave (Smith 1984, 1986) may form within relatively broad fronts interacting with a mountain. Further results may be found in the reviews noted above and the references found therein.

The approaches outlined above cannot adequately describe the interaction of realistic three-dimensional fronts with isolated orography in a stratified fluid. Here, the interaction of an idealized cold front with an isolated mountain ridge is examined by means of a primitive equation channel model. The main goal is to clarify the principal physical mechanisms responsible for the modification of a front during its interaction with isolated orography. The experimental setup is described in section 2. The general shape and orientation of the mountain ridge are chosen to crudely correspond to the Alps, although variations in the profile are used to analyze the interaction in a more general context. The front is associated with a fully nonlinear three-dimensional baroclinic wave that develops in a jet, and it contains most of the basic features found in observed cold fronts (Mudrick 1974). Although Orlanski and Gross (1994) have shown that a lee cyclone is generated when a baroclinic wave and its trailing cold front impinge on an isolated ridge, this development is excluded here by placing the mountain completely outside of the jet. The frontogenetical and frontolytical forcing that occurs as this front interacts with the mountain is evaluated in section 3. The analysis focuses on surface features since the forcing is strongest there. Many of the features present in this interaction are captured by passive scalar simulations of flow over orography (e.g., Blumen and Gross 1987), in agreement with the two-dimensional analysis presented by Williams et al. (1992). However, in this primitive equation model, the principal frontogenetical forcing is provided by distinctly *unbalanced* effects. A significant cross-mountain pressure gradient, that is associated with the blocking of the cold synoptic-scale surface anticyclone by the mountain, provides substantial ageostrophic accelerations and frontogenesis on the lee slope. Stronger fronts (larger temperature contrasts) characterized by higher pressure anomalies and faster propagation speeds tend to be blocked less by the mountain than weaker fronts, as discussed in section 4. The flow may be completely blocked if the mountain is high enough or the front is weak enough, and in these cases the cold air must flow anticyclonically around the east end of the ridge. Conclusions are presented in section 5.

2. Experimental setup

A hydrostatic Boussinesq primitive equation model on an f plane, derived from the "ZETA" model described in the Appendix of Orlanski and Gross (1994), is employed. The version used here is inviscid and adiabatic, except weak second-order horizontal diffusion,

with a coefficient of 5×10^4 m^2 s^{-1}, is included to control noise. The domain is periodic in the zonal direction and is bounded by impermeable walls at the north and south boundaries, a rigid lid at the upper boundary, and idealized orography at the lower boundary. This domain is divided into 97×115 grid points in the horizontal, at a resolution of 42 km, and 33 levels in the vertical. A time step of 300 s is used in the simulations presented here. The vertical terrain-following coordinate is given by

$$Z = e^{-\epsilon[(z-h(x,y))/(H-h(x,y))]}, \qquad (1)$$

where $h(x, y)$ represents the height profile of the isolated mountain and H the height of the rigid lid, set here to 10 km. The parameter ϵ controls the vertical distribution of model levels: larger values of ϵ concentrate model levels near the ground. Additional model details are provided by Orlanski and Gross (1994).

The initial conditions for the simulations presented here consist of a cold front, associated with a nonlinear baroclinic wave, approaching an isolated mountain barrier. The baroclinic wave component of the initial condition is generated over flat terrain by allowing an initial Eady wave perturbation, provided by the analytical linear quasigeostrophic solution, to grow for four days on a zonally symmetric jet. The jet is characterized by a constant vertical shear and is in thermal wind balance with a horizontal potential temperature gradient given by

$$\frac{\partial \Theta}{\partial y} = \begin{cases} -\dfrac{f\Theta_0\Lambda}{2g}\left\{1 + \cos\left[\dfrac{\pi}{L_y}(y - y_0)\right]\right\}, \\ \qquad\qquad\qquad\qquad |y - y_0| \leq L_y \\ 0, \qquad\qquad\qquad |y - y_0| > L_y, \end{cases} \qquad (2)$$

where f is the constant Coriolis parameter, $\Theta_0 = 302$ K is a reference temperature, g is the gravitational constant, and Λ is the constant vertical shear in the jet. The
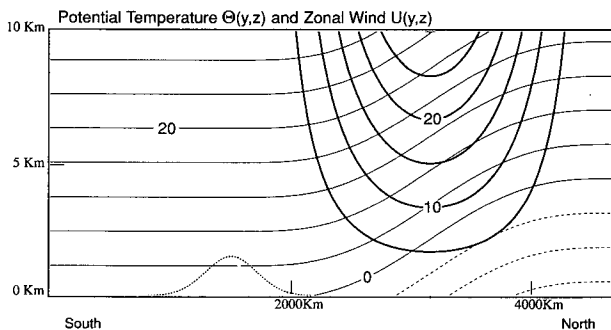

Potential Temperature $\Theta(y,z)$ and Zonal Wind $U(y,z)$

Fig. 2. Potential temperature $\Theta(y, z)$ (thin contours every 4 K) and zonal wind $U(y, z)$ (thick contours every 5 m s^{-1}) in the basic state used for the control simulations. Negative contours are dashed. Tick marks are placed every 2000 km in the horizontal and every 5 km in the vertical. The mountain profile (dotted line) at the middle of the ridge used in the control experiment is shown for reference.
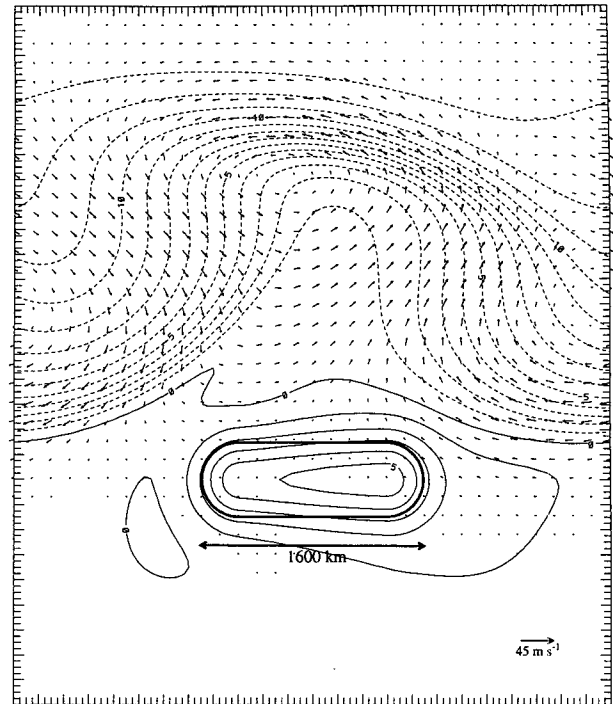

Fig. 3. Surface potential temperature (contours every 1 K) and horizontal velocity at the surface in the control experiment immediately after the injection of the mountain at $t = 0$ h. Negative temperature contours are dashed, and the velocity scale is shown at the lower right corner. The mountain half-height is indicated by the bold closed contour. Tick marks are placed at every grid point (every 42 km).

width of the jet is $L_y = 3000$ km, and y_0 is the location of the jet axis, which is positioned well north of the mountain ridge. The basic-state stratification is characterized by a Brunt–Väisälä frequency of 0.01 s^{-1}. The basic state is shown in Fig. 2.

After the wave has evolved for four days, developing warm and cold fronts are clearly seen in the surface potential temperature and velocity distribution, shown in Fig. 3 for a shear of $\Lambda = 0.003$ s^{-1}. The baroclinic wave has a phase speed of approximately 15 m s^{-1}, and the cold front eventually moves southward and intersects an isolated mountain ridge. This mountain is injected into a relatively quiescent part of the flow, located here in the warm sector of the developing wave, to provide the complete initial condition. In this injection, the mountain replaces, rather than displaces, that part of the domain which the mountain occupies. As a consequence, the mountain intersects isentropic surfaces in the stably stratified atmosphere, as shown in Figs. 2 and 3. It should be noted that when the mountain is inserted in a way that *does* displace the isentropes upward, a mountain anticyclone[1] is required to balance

----

[1] The mountain anticyclone found in steady flow over an isentropic

and maintain the mass distribution (Merkine and Kálnay-Rivas 1976; Blumen and Gross 1987). Since a mountain anticyclone is not necessarily the dominant feature of more general time-dependent flow over a nonisentropic ridge, the initial condition shown in Fig. 3 was adopted for its simplicity.

3. Evaluation of results

A control experiment is examined first to establish the basic characteristics of the interaction between the front and the isolated orography. In this experiment, the mountain is 1500 m high. The north–south cross section is Gaussian with an e-folding width of 600 km, and the east–west profile is a plateau 1000 km long surrounded by Gaussian slopes 300 km wide, for a total e-folding width of 1600 km. The initial state is shown in Fig. 3.

The surface potential temperature and velocity at selected times during the control simulation are shown in Fig. 4. Anticyclonic motion has developed over the ridge after 36 hours of model integration (Fig. 4a) as the relatively strong northerly flow associated with the front passes over the mountain. The potentially warm pool of air initially over the ridge has been advected southward and eastward off the mountain, and has cooled somewhat by weak diffusion in the model. At 48 hours, the flow has accelerated frontal progression to the east of the ridge and retarded it to the west, as shown in Fig. 4b. The associated flow divergence pattern has produced weaker and stronger temperature gradients at the east and west ends of the ridge, respectively. The flow has accelerated and become frontolytical on the windward slope of the mountain as a consequence of mass conservation. These features are similar to those found in the passive scalar simulations of Blumen and Gross (1987).

At 60 hours (Fig. 4c), the front has cleared the south slope of the ridge, and the maximum temperature gradients occur in the front directly south of the mountain. Almost none of the thermal contrast in the front is associated with the potentially warm air initially positioned over the mountain (Fig. 3). Very strong shear and divergence characterize the flow, which reaches a speed of about 45 m s^{-1} in the vicinity of the front. However, the front remains nearly stationary at the west end of the ridge. There, the anticyclonic circulation over the ridge has prevented the cold air from propagating southward as it would in the absence of the mountain (Fig. 4d), and has rotated the isotherms into a north–south orientation over the ridge. In contrast, a distinct southward bulge is seen in the eastern half of the front after it has passed over the ridge. This latter

ridge requires that at some previous point in time the cross-ridge flow was strong enough to establish the isentropic condition at the ground, and as such represents a solution to a particular set of initial value problems, as discussed by Merkine and Kálnay-Rivas.

feature is associated with the upstream deceleration of air by the ridge and the consequent tendency of this air to drift eastward and accelerate southward around the east end of the ridge under the influence of the pressure gradient in the baroclinic wave, as discussed below.

The frontal distortion described here is qualitatively similar to that found in the simulation of two-layer quasigeostrophic flow over a circular mountain presented by Blumen (1992, Fig. 8). However, as will be shown below, ageostrophic advection, neglected in Blumen's depiction, plays the principal role in propelling the front over the ridge. The frontogenesis that takes place during the interaction between the front and the ridge will be examined first.

a. Frontogenetical forcing

Changes in the magnitude of the horizontal gradient of the potential temperature θ may be explicitly evaluated in terms of the frontogenesis function, which in the absence of dissipation may be expressed as (Orlanski et al. 1985)

$$\frac{d}{dt}|\nabla_H\theta| = -\frac{D}{2}|\nabla_H\theta| - \frac{1}{|\nabla_H\theta|}$$

$$\times \left[\frac{\tau}{2}\left(\left(\frac{\partial\theta}{\partial x}\right)^2 - \left(\frac{\partial\theta}{\partial y}\right)^2\right) + \eta\frac{\partial\theta\partial\theta}{\partial x\partial y}\right]$$

$$-\frac{\partial\theta}{\partial z}(\nabla_H w\cdot\hat{e}_n). \quad (3)$$

In (3), D is the horizontal divergence, $\tau = \partial u/\partial x - \partial v/\partial y$ is the stretching deformation, and $\eta = \partial v/\partial x + \partial u/\partial y$ is the shearing deformation. Together these terms represent changes to the horizontal temperature gradient due to contraction of isotherms along a trajectory. The last term on the right-hand side of (3) represents vertical tilting, where $\hat{e}_n$ is the unit vector parallel to the horizontal potential temperature gradient.

The individual terms in (3) have been evaluated along parcel trajectories that pass over the mountain. For example, a suite of surface trajectories associated with a section of the $\theta = -2$ K isotherm is displayed in Fig. 5. These trajectories were calculated by solving

$$\mathbf{X}^{n+1} - \mathbf{X}^n = \Delta\tau\frac{(\mathbf{v}(\mathbf{X}^{n+1}) + \mathbf{v}(\mathbf{X}^n))}{2} \quad (4)$$

for the parcel coordinates $\mathbf{X} = (x, y, Z)$ as a function of the three-dimensional velocity $\mathbf{v}$, where $\Delta\tau = 20$ minutes. A set of trajectories from $t = 36$ h to $t = 60$ h is shown from simulations with the ridge (Fig. 5a) and without it (Fig. 5b). The dotted lines across the trajectories in Fig. 5a indicate the position of the isotherm in panels (a)–(c) of Fig. 4. Anticyclonic curvature is clearly evident in both sets of trajectories; in the absence of the ridge this curvature is due entirely to the anticyclonic circulation within the baroclinic
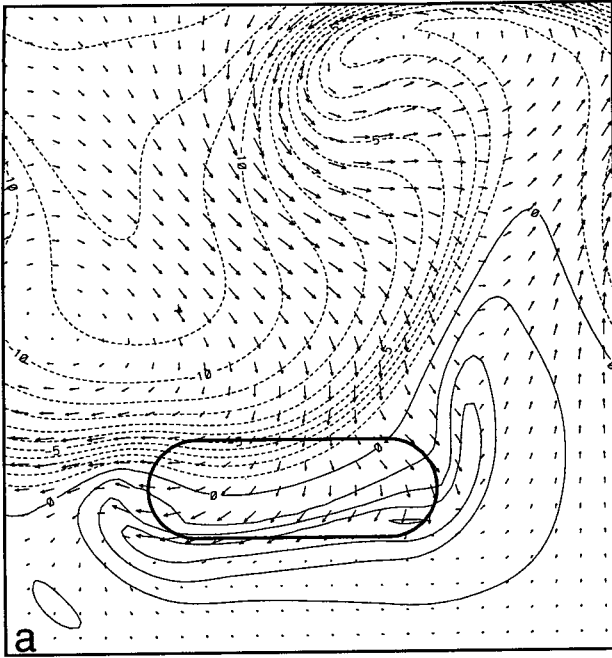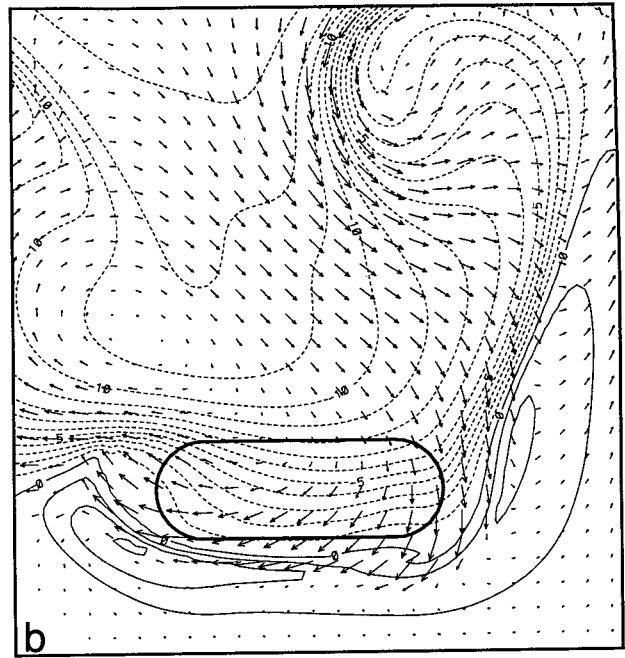
t=36 h

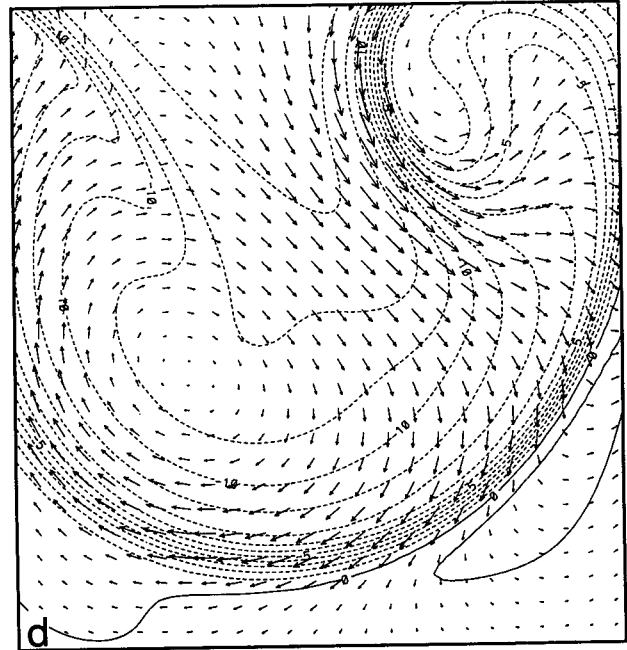t=48 h

45 m s⁻¹
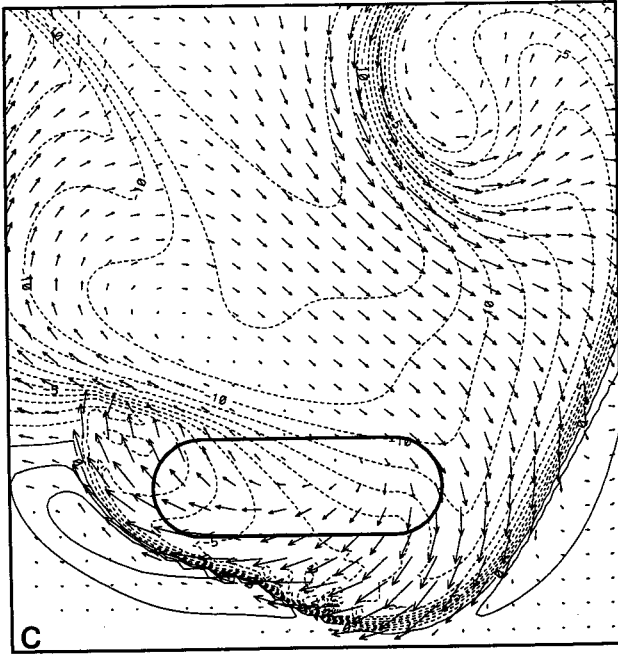
t=60 h

t=60 h (no mountain)

FIG. 4. As in Fig. 3 except at (a) t = 36 h, (b) t = 48 h, and (c) t = 60 h. The fields at t = 60 h in the simulation without the mountain are shown in (d). Only a portion of the domain near the mountain is shown.

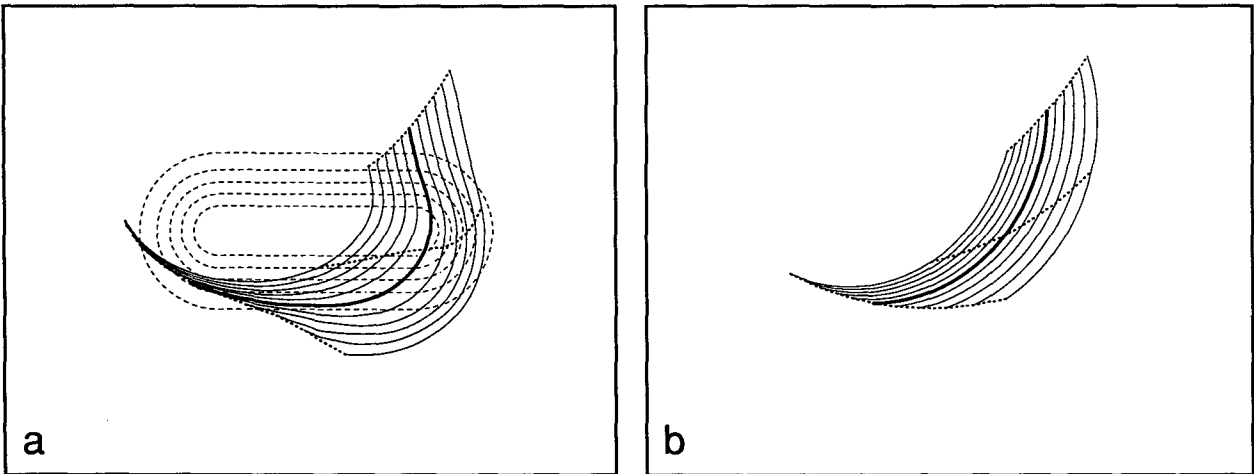# mountain   # no mountain

FIG. 5. Parcel trajectories (solid lines) for a section of the $\theta = -2$ K isentrope (a) with and (b) without the mountain, from $t = 36$ h to $t = 60$ h. Dotted lines indicate the position at $t = 36$ h, 48 h, and 60 h. In (a), the bold line represents the trajectory used in Fig. 6, and the dashed contours are isopleths of height along the mountain, placed every 250 m.

wave, but the larger curvature in the simulation with the mountain results from the production of anticyclonic vorticity as air parcels traverse the ridge. These trajectories indicate that nearly all of the air located directly behind the front in Fig. 4c originated on the northeastern flank of the ridge.

The horizontal potential temperature gradient and the frontogenetical terms in (3) are displayed in Fig. 6

for the trajectory indicated by the heavy line in Fig. 5a. The height of the parcel is also shown for orientation. As this particular parcel ascends the ridge, weak frontolysis diminishes the strength of the front. This frontolysis is due to divergence associated with the acceleration of the flow over the mountain peak, as noted above and shown in Fig. 4b. When the parcel passes over the peak and into the lee, tilting promotes rela-
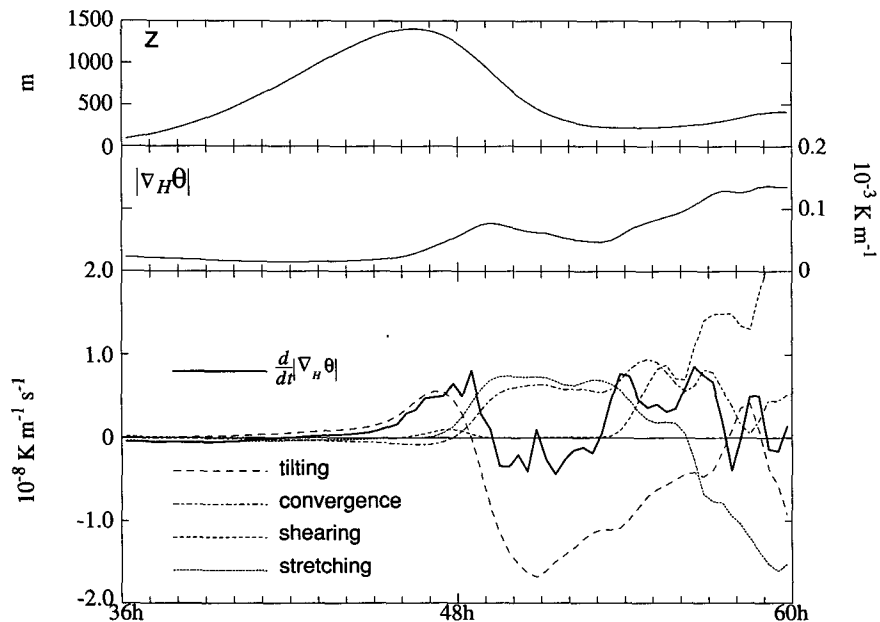

FIG. 6. Parcel height (top), horizontal temperature gradient (middle), and frontogenetical forcing terms (bottom) along the bold trajectory in Fig. 5a.

tively strong frontogenesis. However, once the parcel passes the point of maximum downward velocity on the lee slope, located approximately at the mountain half-width, tilting becomes frontolytical. Frontogenesis provided by convergence and stretching deformation on the lee slope cannot overcome the strong frontolysis due to tilting. This behavior is similar to that previously found in passive scalar simulations of flow over an isolated ridge. In particular, Blumen and Gross (1987) have shown that at this end of the ridge, anticyclonic vorticity enhances the cross-ridge flow and the vertical motion forced by the terrain, producing frontolysis.

Once the front has descended the lee slope, convergence and stretching deformation produce strong frontogenesis, which results in the large temperature gradients seen in Fig. 4c. In fact, the sum of these terms in (3) is proportional to $-(\partial v/\partial y)|\partial\theta/\partial y|$, which clearly is significant over the ridge in Fig. 4b. The enhancement of the temperature gradients by shearing deformation, which is relatively small until the parcel has crossed the ridge and ceased its descent, can also be seen in Fig. 4c, particularly near the southwest flank of the ridge. This forcing is due to the horizontal shear generated as the flow is forced to curve anticyclonically over the ridge, as shown in the trajectories in Fig. 5. It should be noted that the magnitude of the frontogenesis in the absence of the ridge is more than an order of magnitude smaller than the values displayed in Fig. 6, and it is relatively constant along the heavy trajectory shown in Fig. 5b, having achieved a balance with horizontal diffusion. As a consequence, changes in the temperature gradient are insignificant along this trajectory.

Cross sections of the cross-mountain flow v and θ, shown in Fig. 7a, reveal that the frontogenetical forcing due to convergence and stretching deformation is associated with a shallow (~500 m) current accelerating down the lee slope. Significant gravity wave activity is present in the temperature field, and the strong descent on the lee slope is responsible for the frontolytical forcing due to the tilting term there. Purely vertical motion occurs above the head of this current. The propagation speed of the front is approximately 8.5 m s^{-1}, while the flow speed behind and normal to the front is 13 m s^{-1}, and this cross-mountain flow is almost entirely ageostrophic, as shown in Fig. 7b. These results are consistent with a gravity current flowing down the lee slope. However, the relatively course resolution used here cannot truly resolve this small-scale feature, and it is often difficult to separate the gravity current aspects of a front from balanced frontal features (Smith and Reeder 1988).

b. Pressure anomaly

The dramatic acceleration of the flow down the lee slope that causes intense frontogenesis may be examined in the context of the kinetic energy equation for
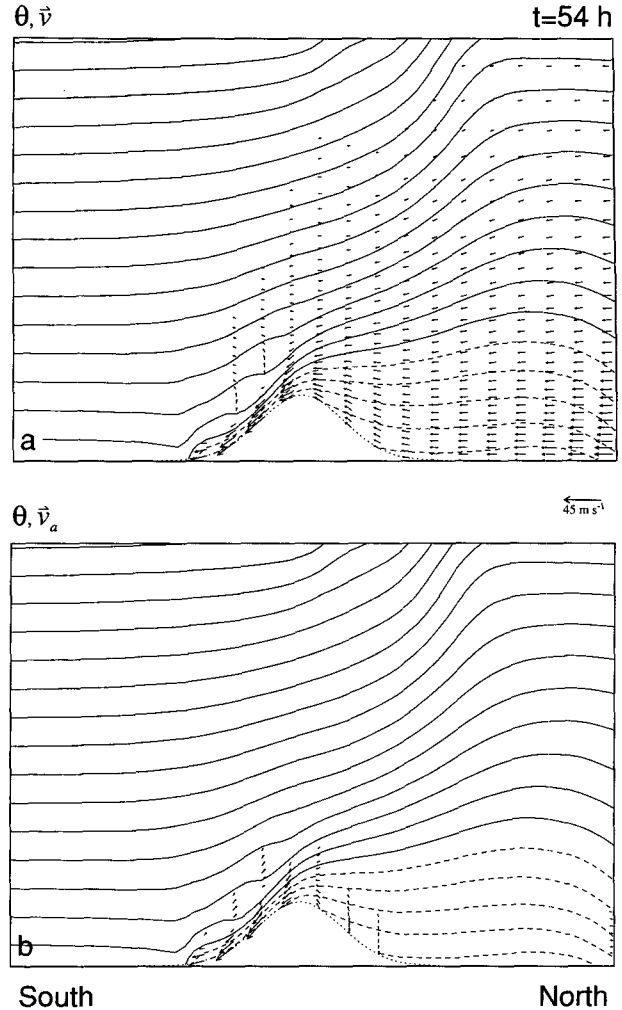

Fig. 7. North–south cross sections at the middle of the ridge of potential temperature (contours every 2 K) and (a) total and (b) ageostrophic cross-ridge velocity at $t = 54$ h.

this Boussinesq model, expressed in the absence of dissipation as

$$\frac{d}{dt}\left(\frac{1}{2}|\mathbf{v}_H\cdot\mathbf{v}_H|\right) = -c_p\Theta_0\mathbf{v}_a\cdot\nabla_H\pi, \qquad (5)$$

where

$$\pi = \left(\frac{p}{p_0}\right)^\kappa, \qquad (6)$$

p is the pressure, the subscript H denotes the horizontal component, and $\mathbf{v}_a$ is the ageostrophic velocity. According to (4), the kinetic energy is changed only by cross-isobaric flow, that is, acceleration by the pressure gradient force along a trajectory. Of course, in this stratified hydrostatic model, the pressure is determined by the distribution of potential temperature in the do-

main, indicating a three-way interplay between the kinetic and potential energies and cross-isobaric flow expressed by the total energy equation

$$\frac{d}{dt}\left(\frac{1}{2}|\mathbf{v}_H\cdot\mathbf{v}_H| - \frac{g\theta z}{\Theta_0}\right) = -c_p\Theta_0\mathbf{v}\cdot\nabla\pi. \quad (7)$$

The importance of ageostrophic flow in defining the energy balance is clearly indicated in (5). However, in balanced models such as those constrained by the geostrophic momentum approximation (Hoskins 1975), the ageostrophic velocity is purely diagnostic. In that case, only the kinetic energy of the geostrophic flow may change through cross-isobaric flow, and the strong ageostrophic flow shown in Fig. 7b will be absent. This point will be considered further in the next section.

In the present solution, a pressure gradient capable of generating the flow observed in Fig. 4 is displayed in Fig. 8, which shows the anomalous pressure and velocity at the surface calculated as the difference between the solutions with and without the mountain. The high pressure anomaly north of the ridge is associated hydrostatically with postfrontal cold air in the baroclinic wave: the mountain decelerates the core of cold air at low levels, while the cold air at upper levels proceeds southward and eastward virtually unaffected. The high pressure anomaly strengthens and travels anticyclonically around the ridge within the cold air. When the cold air is no longer blocked but is allowed to pass southward at the east end of the ridge, substantial flow acceleration takes place and the anomalous pressure gradients along the flow begin to weaken, as shown in Fig. 8c. The structure of the surface pressure at this time is quite similar to that observed in Fig. 1 and in Alpine blocking events (Chen and Smith 1987, in particular their Figs. 5 and 7). Nearly all of the flow in the bulge on the southeast flank of the mountain shown in Fig. 4c is ageostrophic and results from this southward acceleration. This feature appears to be a gravity current flowing around the east end of the ridge, as it is driven primarily by the pressure anomaly shown in Fig. 8, and the flow is directed across the isobars. It is this rapid flow that is responsible for the frontogenetical shearing observed in the southward frontal bulge in Fig. 4c.

A vertical cross section of the pressure and velocity anomaly shows that the pressure anomaly is confined to a Rossby depth $D = fL/N \sim 3$ km based on the mountain half-width L, and the strongest gradients are located at the surface. The cross-isobaric nature of the anomalous flow indicates that the pressure gradients produce strong *ageostrophic* accelerations on the lee slope, as can be seen by comparing the flow there in Figs. 7b and 9. However, this rapid current is too shallow to relieve the buildup of mass north of the ridge, so the high pressure anomaly continues to strengthen, as shown in Fig. 8. Subsidence in the center of the

anomaly and surface divergence are consistent with a gravity current interpretation of the flow anomaly.

In contrast to the rapid progression of the pressure anomaly at the east end of the ridge, the intensifying low pressure anomaly at the west end of the mountain travels only slightly northward and eastward around the ridge. Low pressure is hydrostatically associated with the warm air ahead of the front; the anticyclonic circulation over the mountain prevents the cold air from advancing southward at the west end of the ridge, thereby creating this stationary warm anomaly and associated cyclonic circulation as the baroclinic wave continues to propagate at upper levels.

Although strong cross-isobaric flow constitutes the principal feature of the surface pressure and velocity anomalies displayed in Figs. 8 and 9, these fields also exhibit some of the characteristics of a topographic Rossby wave (Pedlosky 1987, sections 3.16 and 6.15) as the anomaly propagates eastward on the north slope of the ridge. This topographic wave depends on a sloping boundary rather than variations in the Coriolis parameter to provide the ambient potential vorticity gradient required for propagation. In this simulation, it may be excited by the collision of the front and the ridge during which the motion is initiated by the meridional wind field in the baroclinic wave. The vertical extent of the anomaly is approximately one Rossby depth, as noted above, and the phase speed is about $10-15$ m s^{-1}. Further, the associated flow appears to be in approximate balance with the pressure anomaly on the north slope of the ridge. These features are consistent with the analysis of Hsu (1987), who has interpreted observed low-level circulation features around the earth's principal mountain ranges as topographic Rossby waves.

The characteristics of the topographic wave may be further analyzed in a simulation with a zonally symmetric ridge, which allows the pressure anomaly to be examined for an extended period of time without any "leaking" around the ends of the mountain as in Figs. 8b,c. The entire potential temperature signature of the wave over the north slope of the ridge appears to propagate eastward as a topographic Rossby wave (Fig. 10a, cf. Fig. 4c). Pressure anomalies induced by cold air deceleration by the ridge (Fig. 10b) remain on the northern slope, growing in strength as they travel eastward, but they never cross the ridge. Further, there is no analog to the enhanced northerly flow and southward bulge at the east end of the finite ridge in the case of the infinite ridge, which prevents the rapid southward acceleration around the east end of the ridge observed in Fig. 4, and the warm anomaly is no longer trapped against the west end of the ridge, but propagates as part of the topographic wave. The measured phase speed of the anomaly in Fig. 10 is approximately 11 m s^{-1}. This value is very close to that of the linear normal mode (about 10 m s^{-1} for the zonal wavelength indicated in Fig. 10) calculated with this topography in
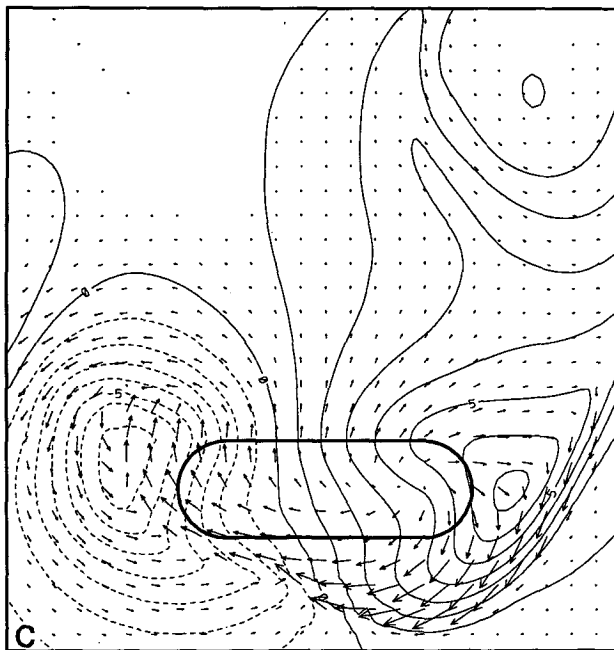
t=36 h
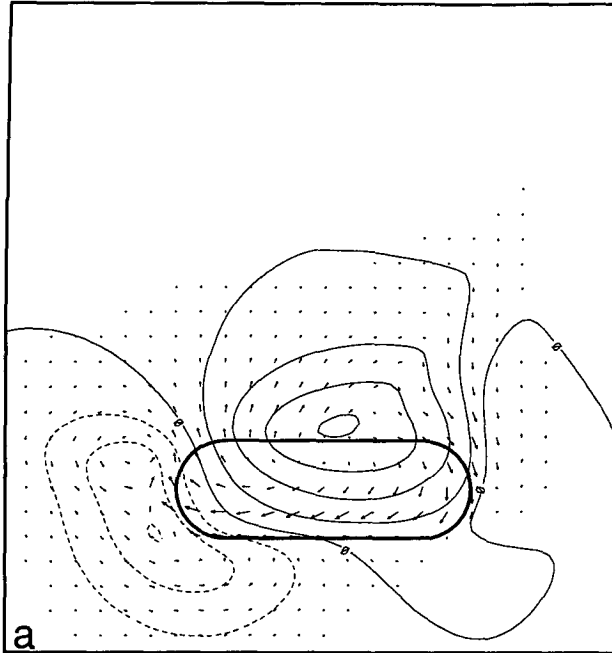
t=48 h
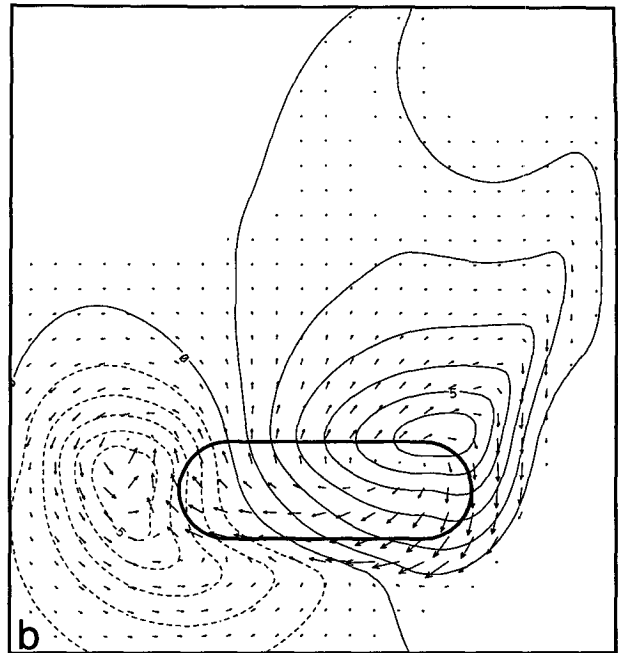
t=60 h

$$\overrightarrow{45\ \mathrm{m\ s^{-1}}}$$

FIG. 8. Anomalous pressure and velocity at the surface at (a) $t = 36$ h, (b) $t = 48$ h, and (c) $t = 60$ h. Contour interval is 1 mb, and negative values are dashed. The mountain half-height is indicated by the bold closed contour.

a resting atmosphere, as might be expected since the zonal wind is quite weak at the ridge.

· Some features of the interaction between the front and topography are independent of the length of the ridge. Intense frontogenesis takes place on the southern slope (Figs. 4 and 10), initiated by convergence and

stretching deformation followed by shearing deformation (Fig. 6). Moreover, the structure of the westward flow behind the front, the curvature of this flow toward the north that arises from the production of anticyclonic vorticity as air parcels cross the ridge, and the potential temperature structure within the western extremity of
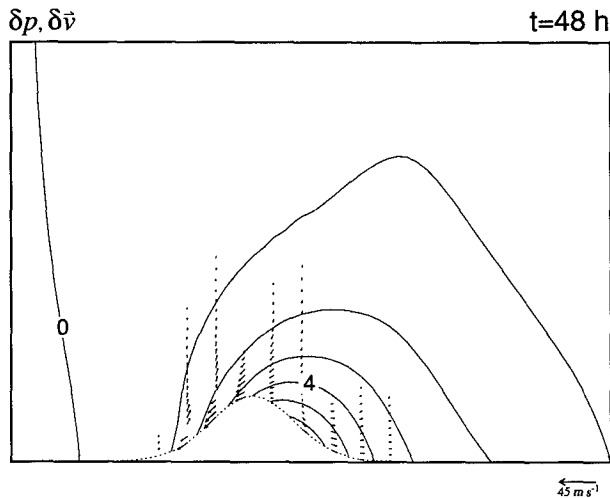
$\delta p, \delta \bar{v}$ t=48 h

FIG. 9. North–south cross section through the maximum pressure anomaly near the east end of the ridge at $t = 48$ h of anomalous pressure and cross-ridge velocity. Contour interval is 1 mb.

this current are all quite similar to their counterparts near the west end of the ridge in Fig. 4c. Evidently, the zonal length of the ridge provides the scale that characterizes the anticyclonic distortion of the front as it passes over the mountain in the control simulation (Fig. 4), but the scale of the distortion is approximately that of the anticyclone in the baroclinic wave when the mountain possesses infinite zonal extent, as shown in Fig. 10, and is much broader than in the case of a finite mountain.

The rapid acceleration of the flow down the lee slope and toward the west and the consequent deformation and divergence patterns that produce the strong temperature gradients in Fig. 4c are the principal responses to the anomalous pressure gradient. As discussed above, kinetic energy increases are associated with accelerations provided by the horizontal pressure gradient along the trajectory. This is consistent with the analysis of Smith (1990), which shows that it is the flow acceleration due to horizontal gradients, rather than conversions between kinetic and potential energy, that determines the nature of steady flow over mountains. Here, the pressure distribution determines the acceleration, and consequent frontogenesis, in the frontal system of the baroclinic wave.

4. Sensitivity of results

The results presented above illustrate a rich variety of features present during the interaction of a front with an isolated ridge. Several aspects of the numerical solution may be further investigated by varying some of the important characteristics of the problem. Schuman (1987) has pointed out that there are seven nondimensional numbers governing the passage of a front over orography in a stratified atmosphere; an exhaustive ex-

ploration of this parameter space will not be undertaken here. Nevertheless, it seems clear that the main features of the above solution, namely, the acceleration of air down the lee slope due to pressure anomalies generated by cold air blocking by the ridge and the deflection of the flow anticyclonically around the east end of the ridge, are associated principally with the mountain height and shape, and the strength of the approaching front. These effects are addressed below.

a. Effects of mountain height

The ability of the mountain ridge to decelerate the cold air behind the front intuitively depends on the

$\theta, \bar{v}$ t=60 h

$\delta p, \bar{v}$ t=48 h
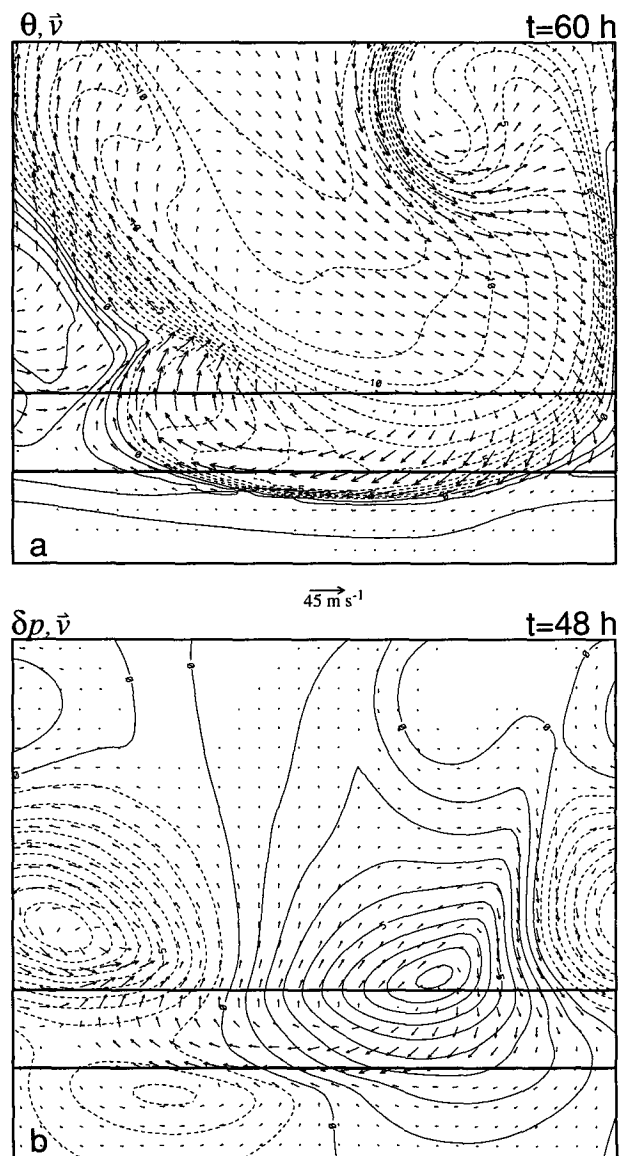

FIG. 10. (a) As in Fig. 4c except for a zonally symmetric ridge.
(b) As in Fig. 8b except for a zonally symmetric ridge.

height of the ridge; a lower mountain will not impede the flow in the front nearly as much as a higher mountain, and the consequent pressure anomalies will be diminished, resulting in weaker frontogenesis. This is confirmed in a simulation with a mountain half as high (750 m) as that shown in Fig. 4. In this case, the strength of the front is only slightly enhanced by its interaction with the mountain, as shown in Fig. 11a. The principal effect is on the position of the front, which is displaced southward and distorted by the anticyclonic vorticity acquired during passage over the ridge. However, this vorticity is weaker and the distortion is less than with the higher mountain shown in Fig. 4c. Further, there is very little evidence that any of the postfrontal air was diverted eastward and around the east end of the ridge, as in Fig. 4c, and the southward bulge on the southeast flank of the ridge is absent here. As a consequence of these latter two features, frontogenesis from shearing deformation (proportional to $\partial\theta/\partial x$) is nearly eliminated in this case.

In stark contrast, model simulations with a ridge 3 km high reveal that nearly all of the cold postfrontal air ($\theta < 0$) is diverted anticyclonically around the east end of the ridge, as shown in Fig. 11b. Almost none of the cold air has ascended past the half-height of 1.5 km, above which remains the warm anomaly that was initially on top of the ridge. The anomalous pressure gradient associated with the blocked low-level cold air north of the ridge cannot build sufficiently to push any air over the high ridge line. Instead, this pressure gradient accelerates the cold air eastward and drives it around the mountain end in a manner similar to a gravity current. As a consequence, the cold front only appears on the eastern half of the lee side in truncated form, as has been observed in fronts blocked by the Alps (e.g., Godske et al. 1957). However, the shape of the front in this case is very similar to that of the front in the eastern half of the lee of the 1.5-km mountain shown in Fig. 4c, which supports the hypothesis that the bulge in this latter feature arises from the advection of cold air *around* the mountain. In the Alpine region, this deflected flow is a key component in establishing the Yugoslavian bora (Smith 1986b).

Since the higher mountain completely blocks the cold air, the low-level static stability behind the front is relatively large. As a consequence of potential vorticity conservation, the anticyclonic vorticity acquired by air parcels as they ascend and pass over the eastern shoulder is greater than that for the 1.5-km mountain, so the parcel trajectories curve northward with the higher mountain rather than take the more westward trajectories shown in Fig. 5a. However, the ridge is high enough that the current of cold air approaching the ridge from the south in Fig. 11b is eventually deflected westward and continues to flow around the south slope of the ridge at later times.

The nature of the distinct current that flows around the ridge in Fig. 11b is of some interest, although a rigorous analysis will not be presented here. There are some similarities between the deflected current in the present simulation and the observationally (Chang et al. 1983) and numerically (Nakamura and Doutani 1985) analyzed cold surges around the Tibetan Plateau. In both cases, there are strong ageostrophic winds immediately behind the front at the head of the current, which is about 1–2 km deep. The current propagates with a speed of 25–30 m s^{-1}, which compares favorably with the estimated phase speed of a Kelvin wave in this parameter range, consistent with the analysis of Hsu (1987). Even so, it may not be possible to distinguish between a Kelvin wave and features that are more characteristic of a rapidly propagating gravity current. Reason and Steyn (1992) have presented a solution that is comprised of both. However, it is not clear that this provides a completely satisfactory description of the current shown in Fig. 11b, which appears to separate from the ridge and hence would be unable to support Kelvin waves. Furthermore, Nakamura and Doutani (1985) point out that the scales under consideration (here, the mountain width and deformation radius are approximately the same) allow topographic Rossby waves to potentially influence the flow evolution; this was indeed observed in the simulations presented in section 3. Finally, it is difficult for the hydrostatic simulation to capture the separation between the pressure surge and cold air that is observed by Chang et al. (1983). These issues remain for future consideration.

The simulations presented in Figs. 4 and 11 illustrate a transition between flow over and flow around an isolated mountain as the ridge height increases. According to the hypothesis presented above, this transition reflects the different degrees of frontal blocking and anomalous pressure gradient generation for different ridge heights. When the flow *does* cross the ridge, a higher mountain (and stronger anomalous pressure gradient) produces more intense frontogenesis. If it is the pressure gradient that determines the nature of the interaction of the front with the mountain ridge, increasing the temperature contrast in the approaching front should enhance the pressure anomaly and strengthen the cross-ridge flow in a manner similar to decreasing the mountain height. This is considered next.

b. Strength of front

Changing the strength of the front in the baroclinic wave is accomplished by changing the maximum shear Λ in the jet and by (2) the maximum meridional potential temperature gradient. The zonal phase speeds of the baroclinic wave are kept the same by changing the magnitude of the surface flow. However, this should have minimal impact in the present simulations, since the mountain is placed outside of the jet. Although comparisons between experiments will be made when the baroclinic wave is in approximately the same position relative to the mountain, the different growth

h=750 m   h=3000 m

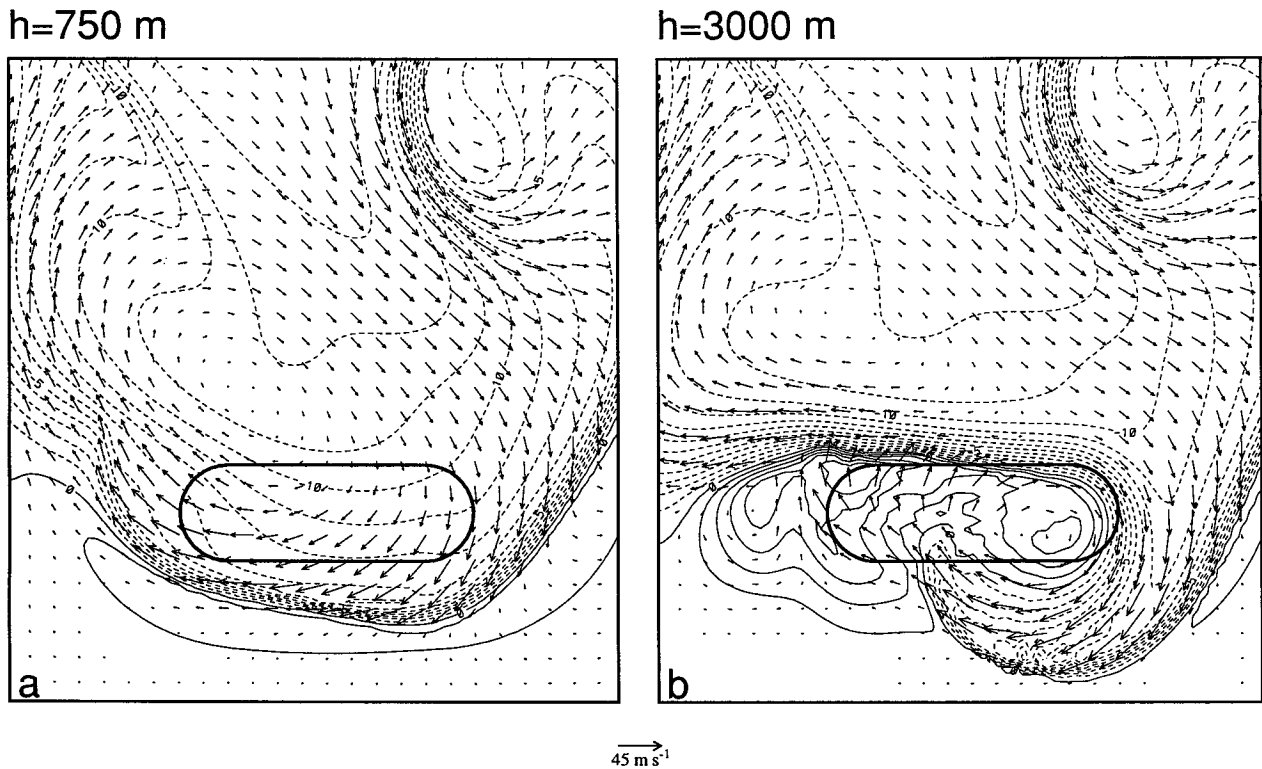$\overrightarrow{45\,m\,s^{-1}}$

FIG. 11. As in Fig. 4c except for mountain heights of (a) 750 m and (b) 3000 m.

rates achieved with different shears do change the southward propagation speed of the cold front and the time at which it encounters the ridge.

A weaker front will possess weaker cross-frontal circulations and produce weaker anomalous pressure gradients when the front approaches the mountain. In this case, the pressure anomaly produced by cold air blocking may be insufficient to push the front over the ridge, so that the flow will be deflected eastward around the end of the ridge. This is confirmed in a simulation in which the shear is reduced from 0.003 s^{-1} to 0.002 s^{-1} but the mountain height remains the same (1.5 km). As shown in Fig. 12a, the front is completely blocked at the west end of the mountain, and a distinct current similar to that in Fig. 11b flows around the east end of the ridge. The distortion of this part of the front is also similar to the southward extension of the front in Fig. 11b and to the southward bulge in the eastern half of the front shown in Fig. 4c, supporting the idea that this latter feature is associated with flow around the end of the mountain.

When the shear is increased to 0.004 s^{-1}, the anomalous pressure gradients are strong enough to push the front over the ridge. In this case, the front is distorted in a manner similar to that in Fig. 11a with a lower mountain and a weaker front. The southward bulge at the east end of the front is less prominent, as a smaller fraction of air is forced to flow around the end of the

ridge (at later times, however, the coldest postfrontal air does flow around rather than over the ridge). The results shown in Figs. 11 and 12 support the hypothesis that the strength of the anomalous pressure gradient that develops from cold air deceleration determines whether the front propagates over the ridge.

In summary, both high mountains and weak fronts tend to produce flow around rather than over the ridge. This is consistent with the analytic steady solution presented by Blumen and Gross (1987), which shows that flow can be blocked with high isentropic mountains or weak incident flow, the latter associated here with small shear in the basic flow Λ and a weak front in the baroclinic wave. In these cases, the pressure gradient generated by blocking cold postfrontal air is insufficient to propel the front over the ridge. The solutions presented above appear to transit smoothly from flow over to flow around the ridge.

It is difficult to determine the critical ridge height above which the front will be totally blocked because the time-dependent nature of the flow precludes application of blocking criteria derived from steady solutions (e.g., Smith 1990), which may not characterize even the basic properties of the flow (Merkine and Kálnay-Rivas 1976). Nevertheless, some progress in understanding the relationship between frontal strength, mountain height, and flow blocking can be made by considering simple Froude number arguments. Here,
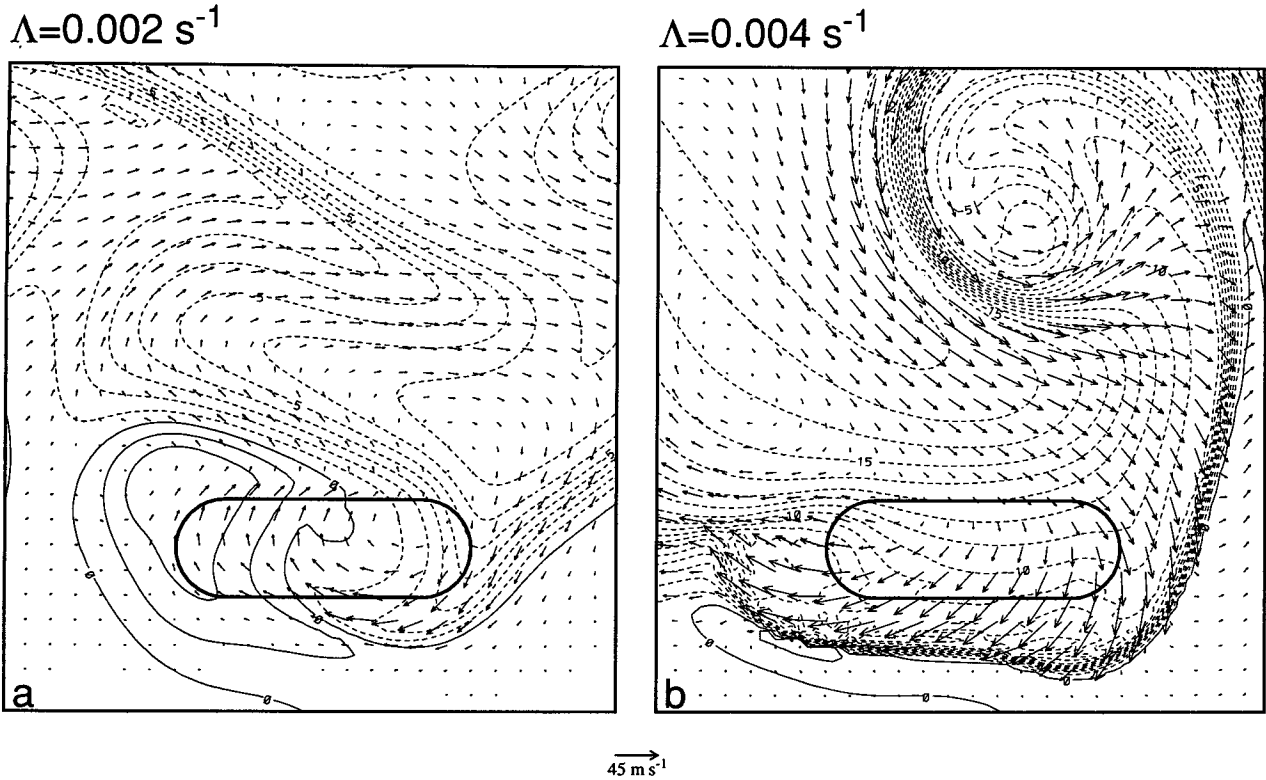
Λ=0.002 s^{-1} Λ=0.004 s^{-1}

$\overrightarrow{45\ m\ s^{-1}}$

FIG. 12. As in Fig. 4c except for vertical wind shears of (a) 0.002 s^{-1} and (b) 0.004 s^{-1}.

the Froude number is defined by Fr $= V_f/Nh$, where V_f is the southward propagation speed of the front and, except for confluence effects, the speed of the air behind it. In these simulations, V_f is determined by the growth of the baroclinic wave. If we approximate V_f by exponential growth characteristic of the linear Eady wave solution, $V_f \sim V_0 e^{\sigma t}$ where $\sigma \sim f\Lambda/N$ is the

FIG. 13. Regime plot of Fr versus R.
The figure corresponding to each point is also indicated.

growth rate. The time τ taken to travel a distance λ to the mountain ridge is $\tau \sim (1/\sigma) \ln(\sigma\lambda/V_0 + 1)$ so that $V_f \sim \sigma\lambda$ and Fr $\sim \Lambda f \lambda/N^2 h$ when $\sigma\lambda \gg V_0$. A reasonable measure of blocking, motivated by the results presented in Figs. 4, 11, and 12 and the accompanying discussion, is provided by the ratio R of the average mass flux around the east end of the ridge to that over the peak. A plot of the Froude number versus R for the simulations presented here (Fig. 13) confirms that higher mountains and weaker fronts, which are both characterized by relatively small Froude numbers, are associated with higher values of R and increased blocking. These results agree qualitatively with the analysis of upstream blocking presented by Pierrehumbert and Wyman (1985, Fig. 14) for stratified flow over an infinite ridge. Although their analysis does not include a front, there is a clear correspondence between the Froude numbers based on their basic-state incident flow speed and on the propagation speed of the front in this analysis.
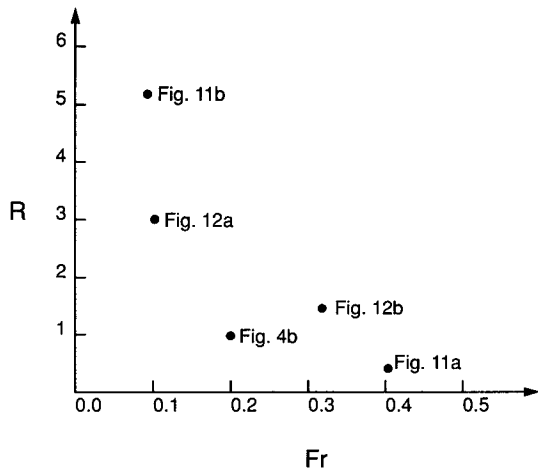
c. Flow balance

Strong frontogenesis in the lee of the ridge and the current that flows around its east end are associated primarily with ageostrophic motion according to Figs. 7b and 8. This response represents the generation of thermal wind imbalance during the interaction of the

$$\vec{v}_a$$

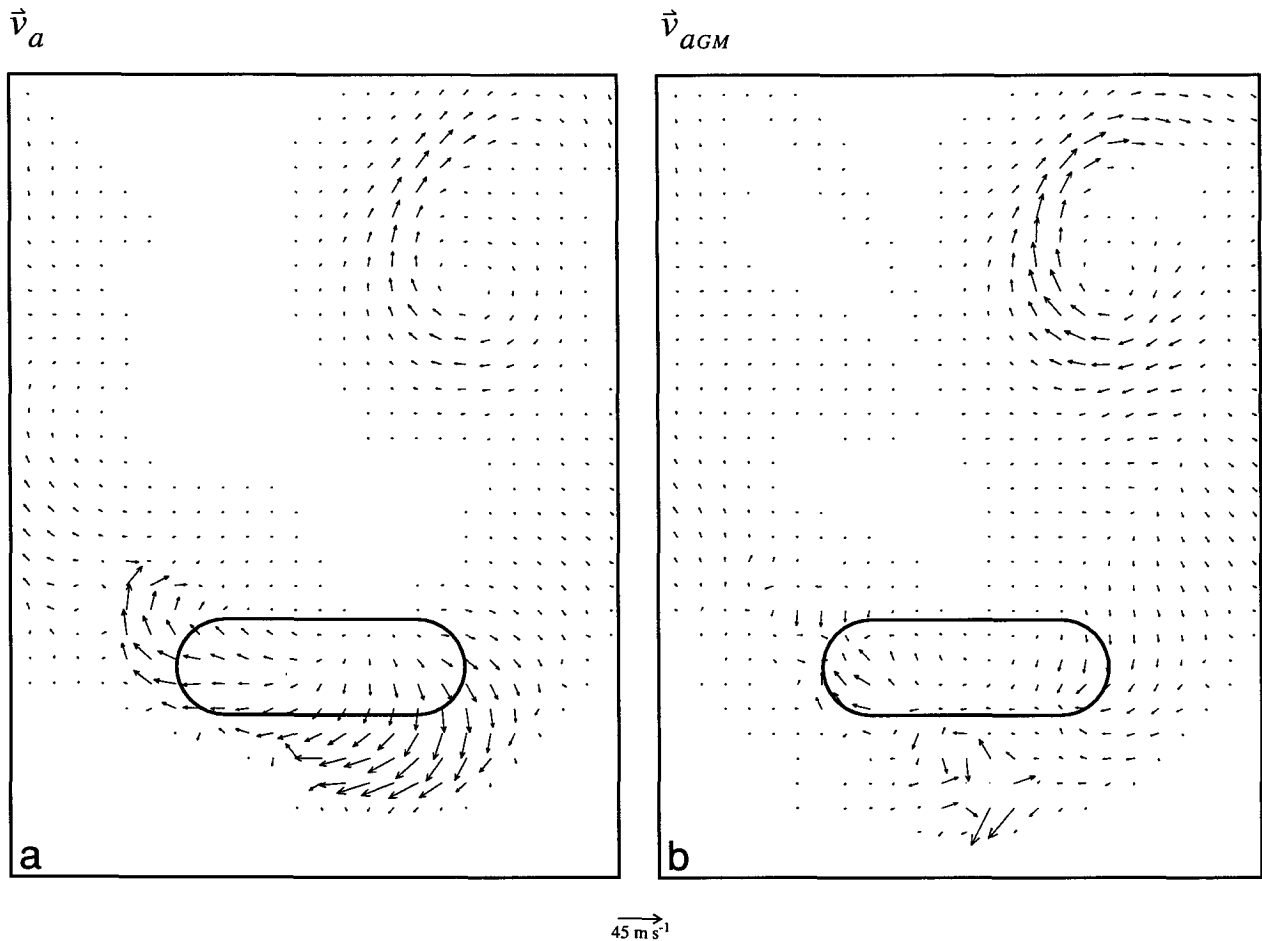$$\vec{v}_{aGM}$$

$$\overrightarrow{45\ m\ s^{-1}}$$

Fig. 14. Ageostrophic wind at $t = 60$ h calculated (a) without and (b) with the geostrophic momentum approximation. The mountain half-height is indicated by the bold closed contour.

front and the ridge. Orlanski and Ross (1977) have shown that this imbalance represents a source of cross-stream vorticity and may intensify the cross-frontal circulation in a manner consistent with Figs. 4b and 7. Note that in a balanced model described, for example, by semigeostrophy, the ageostrophic flow would maintain thermal wind balance in the front even in the presence of the anomalous pressure gradient, and the rapid downslope accelerations resulting in the strong ageostrophic cross-front flow shown in Fig. 7b would most likely be absent.

These considerations may be quantitatively assessed by examining the difference between the actual fluid accelerations dv/dt and those that would occur when the geostrophic momentum approximation, $dv/dt \approx dv_g/dt$ (Hoskins 1975), is made. These accelerations were calculated between consecutive model time steps to minimize truncation error, and are expressed in terms of the instantaneous ageostrophic velocities

$$v_a = k \times \frac{1}{f} \frac{dv}{dt} \tag{8}$$

and

$$v_{aGM} = k \times \frac{1}{f} \frac{dv_g}{dt} \tag{9}$$

for ease of comparison with Fig. 4. Note that (8) is simply the horizontal momentum equation in the absence of dissipation. These velocities at the surface are shown in Fig. 14 at a time corresponding to Fig. 4b.

The ageostrophic circulations calculated from (8) and (9) in the low pressure system of the baroclinic wave (upper right corner of Figs. 14a,b, respectively) are quite similar, with the geostrophic momentum approximation slightly overestimating the magnitude of the ageostrophic vorticity. As a consequence, the total circulation $v_g + v_{aGM}$ in the low is weaker than in the full primitive equation solution, consistent with the
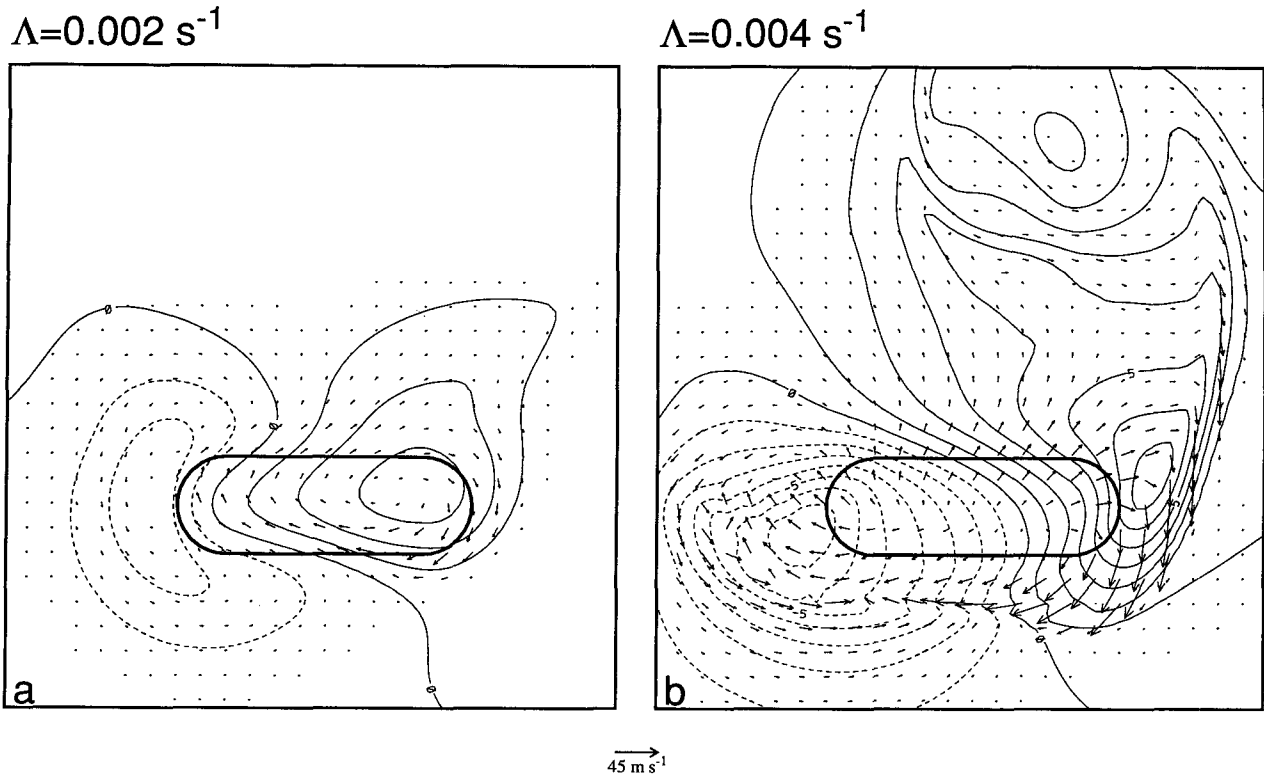
Λ=0.002 s^{-1} Λ=0.004 s^{-1}

$\overrightarrow{45\ \mathrm{m\ s}^{-1}}$

FIG. 15. As in Fig. 8c except for vertical wind shears of (a) 0.002 s^{-1} and (b) 0.004 s^{-1}.

analysis of Snyder et al. (1992). In most other regions of the domain away from the mountain, the two solutions are also similar, as would be expected with the scales under consideration here.

However, near the mountain the two solutions are quite different, indicating a substantial degree of imbalance in the flow. The flow over the mountain shown in Fig. 14a compares favorably with that in Fig. 4c, confirming that most of the flow behind the front is ageostrophic. Indeed, the ageostrophic flow calculated with (8) and by the simple residual $\mathbf{v} - \mathbf{v}_g$ are nearly identical, with the absence of dissipation in (8) accounting for the difference. In contrast, the balanced ageostrophic flow over the ridge in Fig. 14b bears little resemblance to the true flow behind the front, and the strong ageostrophic downslope flow is absent. This is not too surprising, as the flow is almost totally ageostrophic here, and the ageostrophic flow (9) determined by changes in the weak geostrophic velocity may be expected to be grossly in error in these regions. Even though the horizontal scales of the anomalous pressure gradients shown in Fig. 8 are a Rossby radius or larger, the depth of the ageostrophic current flowing over the ridge, shown in Fig. 7, is much less than a Rossby depth, also indicating that the region behind the front is one of strong imbalance.

It is also apparent from an examination of the pressure and velocity anomalies associated with the flows

in Fig. 12, shown in Fig. 15, that there is strong imbalance when the shear Λ and front are strong, as indicated by the substantial cross-isobaric flow in Fig. 15b. Since it is essentially the Lagrangian time scale that determines the validity of the geostrophic momentum approximation used in (9) (Hoskins 1975), the interaction of the strong front, characterized by larger growth rates in the baroclinic wave and faster propagation speeds V_f, with the mountain has a shorter characteristic interaction time L/V_f and less time for geostrophic adjustment to operate.

5. Conclusions

The interaction of an idealized cold front with isolated orography has been considered. Despite the relative complexity of the flow examined here, some features of this interaction, including frontolysis on the windward slope, frontogenesis on the lee slope, and anticyclonic deformation of the front after passage over the mountain, compare well with passive scalar simulations (e.g., Blumen and Gross 1987). Williams et al. (1992) reached a similar conclusion for the analogous two-dimensional interaction. The dependence of blocking on a Froude number, here based on the strength of the baroclinic wave and the height of the mountain, qualitatively agrees with earlier results derived from simulations of stratified flow over an infinite ridge

(Pierrehumbert and Wyman 1985). However, several additional features emerge in the three-dimensional time-dependent simulations presented here.

When the mountain is low enough or the approaching front is strong enough (large Froude number), the mountain impedes propagation of the synoptic high pressure behind the front, thereby generating a high pressure anomaly north of the ridge and a consequent cross-mountain pressure gradient. The flow over the ridge responds to this pressure gradient by accelerating rapidly down the lee slope, producing intense confluence and frontogenesis. The pressure anomaly propagates eastward in a manner similar to a topographic Rossby wave until it reaches the end of the ridge, when the anomalous pressure gradients produce strong ageostrophic flow around the ridge, as in a gravity current.

However, when the mountain is high or the front weak (small Froude number), the front and the flow behind it may be completely blocked. In this case, the anomalous pressure gradient forces the postfrontal cold air to flow eastward and southward around the east end of the mountain ridge. This solution possesses features similar to those seen in cold surges around the east side of the Tibetan Plateau. In both cases, the flow immediately behind the front possesses substantial imbalance even though the horizontal scales are of the order of a deformation radius, and may be characterized as a gravity current.

Some of the principal features of observed frontal interactions with orography may be captured by this relatively simple model. For example, the eastward propagation of the front along the north side of the Alps, shown in Fig. 1a, is closely mimicked by the numerical solution with a 3-km ridge. However, it is clear that the shallow nature of the cross-ridge current shown in Fig. 7, and the surface flow shown in Fig. 4, may be substantially altered in the presence of realistic terrain or boundary layers. For example, Smith (1986b) has proposed that the development of the mistral may be qualitatively explained in part by the acceleration of the flow down the Rhone valley by an anomalous pressure gradient similar to that shown in Fig. 8. However, he also notes that surface friction may play an important role in limiting the flow that arises from this mechanism. Neither small-scale topographic features nor surface friction has been included in the present simulations. Also, these experiments use idealized fronts that do not contain certain important features, such as well-confined stable layers, that are observed in atmospheric fronts. Finally, as noted at the beginning of section 4, the sensitivity of the present results to several additional flow characteristics is not considered here. For example, the frontogenetical forcing shown in Fig. 6 would clearly be different for different ridge orientations relative to the incident front. These subjects represent the focus of future research.

REFERENCES

Blumen, W., 1992: Propagation of fronts and frontogenesis versus frontolysis over orography. *Meteorol. Atmos. Phys.,* **48,** 37–50.

——, and B. D. Gross, 1987: Semigeostrophic flow over orography in a stratified rotating atmosphere. Part I: Steady three-dimensional solutions over finite ridges. *J. Atmos. Sci.,* **44,** 3007–3019.

Chang, C.-P., J. E. Erickson, and K. M. Lau, 1979: Northeasterly cold surges and near-equatorial disturbances over the winter MONEX area during December 1974. Pat I: Synoptic aspects. *Mon. Wea. Rev.,* **107,** 812–829.

——, J. E. Millard, and G. T. J. Chen, 1983: Gravitational character of cold surges during winter MONEX. *Mon. Wea. Rev.,* **111,** 293–307.

Chen, W. D., and R. B. Smith, 1987: Blocking and deflection of airflow by the Alps. *Mon. Wea. Rev.,* **115,** 2578–2597.

Davies, H. C., 1984: On the orographic retardation of a cold front. *Beitr. Phys. Atmos.,* **57,** 409–418.

Egger, J., and K. P. Hoinka, 1992: Fronts and orography. *Meteorol. Atmos. Phys.,* **48,** 3–36.

Godske, G. L., T. Bergeron, J. Bjerknes, and R. C. Bundgaard, 1957: *Dynamic Meteorology and Weather Forecasting.* Amer. Meteor. Soc., 800 pp.

Hartjenstein, G., and R. Bleck, 1991: Cold air outbreak along the eastern rim of the Rocky mountains. *Mon. Wea. Rev.,* **109,** 2280–2292.

Hoinka, K. P., and H. Volkert, 1987: The German Front Experiment 1987. *Bull. Amer. Meteor. Soc.,* **68,** 1424–1428.

——, and D. Heimann, 1988: Orographic channeling of a cold front by the Pyrenees. *Mon. Wea. Rev.,* **116,** 1817–1823.

——, M. Hagen, H. Volkert, and D. Heimann, 1990: On the influence of the Alps on a cold front. *Tellus,* **42A,** 140–164.

Hoskins, B. J., 1975: The geostrophic momentum approximation and the semi-geostrophic equations. *J. Atmos. Sci.,* **32,** 233–242.

Hsu, H. H., 1987: Propagation of low-level circulation features in the vicinity of mountain ranges. *Mon. Wea. Rev.,* **115,** 1864–1892.

Koch, S. E., and P. J. Kocin, 1991: Frontal contraction processes leading to the formation of an intense narrow rainband. *Meteorol. Atmos. Phys.,* **46,** 123–154.

Merkine, L. O., and E. Kálnay-Rivas, 1976: Rotating stratified flow over finite isolated topography. *J. Atmos. Sci.,* **33,** 908–922.

Mudrick, S. E., 1974: A numerical study of frontogenesis. *J. Atmos. Sci.,* **31,** 869–892.

Nakamura, H., and T. Doutani, 1985: A numerical study on the coastal Kelvin wave features about the cold surges around the Tibetan Plateau. *J. Meteor. Soc. Japan,* **63,** 547–563.

Orlanski, I., and B. B. Ross, 1977: The circulation associated with a cold front. Part I: Dry case. *J. Atmos. Sci.,* **34,** 1619–1633.

——, and B. D. Gross, 1994: Orographic modification of cyclone development. *J. Atmos. Sci.,* **51,** 589–611.

——, B. Ross, L. Polinsky, and R. Shaginaw, 1985: Advances in the theory of atmospheric fronts. *Advances in Geophysics,* Vol. 28B, Academic Press, 223–252.

Pedlosky, J., 1987: *Geophysical Fluid Dynamics,* second ed., Springer-Verlag, 710 pp.

Pierrehumbert, R. T., and B. Wyman, 1985: Upstream effects of mesoscale mountains. *J. Atmos. Sci.,* **42,** 977–1003.

Radinovic, D., 1986: Analyses of ALPEX data, 20, 21 March and 24, 25, 30 April 1982. PSMP Report Series 22, WMO/TD No. 154.

Reason, C. J. C., and D. G. Steyn, 1992: The dynamics of coastally trapped mesoscale ridges in the lower atmosphere. *J. Atmos. Sci.,* **49,** 1677–1692.

Schär, C., 1990: Quasi-geostrophic lee cyclogenesis. *J. Atmos. Sci.,* **47,** 3044–3066.

Schumann, U., 1987: Influence of mesoscale orography on idealized cold fronts. *J. Atmos. Sci.,* **44,** 3423–3441.

Smith, R. B., 1979: The influence of mountains on the atmosphere. *Advances in Geophysics,* Vol. 21, Academic Press, 87–230.

——, 1984: A theory of lee cyclogenesis. *J. Atmos. Sci.,* **41,** 1159–1168.

——, 1986a: Further development of a theory of lee cyclogenesis. *J. Atmos. Sci.,* **43,** 1582–1602.

——, 1986b: Mesoscale meteorology in the Alps. Scientific Results of the Alpine Experiment. Vol. II, GARP Pub. Ser. 27, WMO/TD No. 108, 407–423.

——, 1990: Why can't stably stratified air rise over high ground? *Atmospheric Processes over Complex Terrain.* W. Blumen, Ed., Amer. Meteor. Soc., 105–107.

Smith, R. K., and M. J. Reeder, 1988: On the movement and low-level structure of cold fronts. *Mon. Wea. Rev.,* **116,** 1927–1944.

Snyder, C., W. C. Skamarock, and R. Rotunno, 1991: A comparison of primitive-equation and semigeostrophic simulations of baroclinic waves. *J. Atmos. Sci.,* **48,** 2179–2194.

Tafferner, A., 1990: Lee cyclogenesis resulting from the combined outbreak of cold air and potential vorticity against the Alps. *Meteorol. Atmos. Phys.,* **43,** 31–47.

Williams, R. T., M. S. Peng, and D. A. Zankofski, 1992: Effects of topography on fronts. *J. Atmos. Sci.,* **49,** 287–305.

Zehnder, J. A., and P. R. Bannon, 1988: Frontogenesis over a mountain ridge. *J. Atmos. Sci.,* **45,** 628–644.